



Effective segmentation and classification for HCC biopsy images

Po-Whei Huang*, Yan-Hao Lai

Department of Computer Science and Engineering, National Chung Hsing University, 250 Kuo Kuang Rd., Taichung 40227, Taiwan, ROC

ARTICLE INFO

Article history:

Received 7 October 2008

Received in revised form

17 February 2009

Accepted 19 October 2009

Keywords:

HCC biopsy image

Morphological grayscale reconstruction

k-nearest neighbor

Support vector machine

Feature selection

Decision-graph

ABSTRACT

Accurate grading for hepatocellular carcinoma (HCC) biopsy images is important to prognosis and treatment planning. In this paper, we propose an automatic system for grading HCC biopsy images. In preprocessing, we use a dual morphological grayscale reconstruction method to remove noise and accentuate nuclear shapes. A marker-controlled watershed transform is applied to obtain the initial contours of nuclei and a snake model is used to segment the shapes of nuclei smoothly and precisely. Fourteen features are then extracted based on six types of characteristics for HCC classification. Finally, we propose a SVM-based decision-graph classifier to classify HCC biopsy images. Experimental results show that 94.54% of classification accuracy can be achieved by using our SVM-based decision-graph classifier while 90.07% and 92.88% of classification accuracy can be achieved by using *k*-NN and SVM classifiers, respectively.

© 2009 Elsevier Ltd. All rights reserved.

1. Introduction

Liver cancer is the fifth most common cancer in the world and the primary cause of cancer related deaths especially in Southeast Asia and tropical Africa. The liver is made up of different cell types (for example, bile duct, blood vessels, and fat-storing cells). However, liver cells (hepatocytes) make up 80% of the liver tissue. Thus, the majority of primary liver cancers (over 90–95%) arises from liver cells and is called hepatocellular carcinoma (HCC).

The diagnosis of HCC is typically performed by blood tests or imaging techniques such as ultrasound, computer tomography (CT), and magnetic resonance imaging (MRI). However, a common method to verify the diagnosis of HCC is through needle biopsy, which takes some cells or a small piece of tissue from the affected area of the liver for analysis under a microscope.

By viewing the microscopic images of biopsy specimens, pathologists can determine the histological grade of HCC. Since prognosis and medical treatments are different with respect to different degrees of HCC malignancy, it is very important to determine the grades for HCC biopsy images accurately. Edmondson and Steiner [1] proposed a grading system commonly used in evaluating the malignancy of HCC on a scale from 0 to 4 based on the degree of differentiated liver cells. From the result of HCC grading, pathologists know how aggressive the cancer is likely to be and how quickly it may spread to other organs. At present, most diagnosis of cancer is still done by visual examination of

imaging studies in a qualitative manner. However, human visual grading for HCC biopsy images is very time-consuming, subjective, and inconsistent due to inter- and intra-observer variations. A more quantitative and reproducible approach for analyzing biopsy images is highly desired. Therefore, the goal of this research study is to develop a computer-aided system for automatically analyzing and correctly grading HCC biopsy images to provide quantitative, more objective, and consistent information for prognosis and treatment planning.

Automatic grading of pathological images has been investigated in various fields during the past few years, including brain tumor astrocytomas (ASTs) [2–5], prostate carcinoma [6–9], and renal cell carcinoma (RCC) [10–14]; however, an automated system for grading HCC biopsy images has not been reported in the literature. Since the grading system for a specific type of cancer cannot be applied to other types of cancers, it is necessary to exploit appropriate segmentation, feature extraction, and classification methods for different types of cancers. This is particularly true for the liver cancer because HCC biopsy images always suffer from the problem of impurities, undesirable elements, and uneven exposure. In HCC grading, the characteristics of nuclei are the key to estimate the degree of HCC malignancy. However, the areas of nuclei, cytoplasm, and cells are difficult to be identified and measured. In this paper, we propose a novel method to transform a segmented HCC biopsy image to a minimum spanning tree (MST) [15] so that the sizes of cells, nuclei, and cytoplasm as well as the mean distance between two nearest neighboring nuclei can be estimated. Fourteen features are extracted from HCC biopsy images according to six types of characteristics commonly adopted by pathologists.

* Corresponding author. Tel.: +886 4 2286 1528; fax: +886 4 2285 3870.
E-mail address: powhei.huang@msa.hinet.net (P.-W. Huang).

We use k -NN, SVM, and SVM-based decision-graph classifiers to test the effectiveness of classification for HCC biopsy images. In this study, we find that not all 14 features are equally important or necessary to distinguish a specific grade from others. Therefore, we propose a specially designed classifier, called SVM-based decision-graph classifier, in which each decision node is associated with a support vector machine and an optimal subset of features so that the best performance of classifying HCC biopsy images can be achieved. A collection of 804 HCC biopsy images acquired from more than 100 patients was used for experiment, where 200 images were used as the training samples and the remaining 604 images were used as the testing images. Experimental results show that the classification accuracy can achieve up to 90.07%, 92.88%, and 94.54% by using k -NN, SVM, and our SVM-based decision-graph classifiers, respectively.

The remainder of the paper is organized as follows. Section 2 presents an overview for segmentation and classification related to this research work. Section 3 describes the image acquisition procedure and the preprocessing steps suitable for HCC biopsy images. Section 4 shows our method for nuclei segmentation. Then, 14 features are defined and the related feature extraction methods are described in Section 5. An SVM-based decision-graph classifier is proposed for grading HCC biopsy images in Section 6. Experimental results to demonstrate the effectiveness of our SVM-based decision-graph classifier as well as comparisons to k -NN and SVM classifiers are presented in Section 7. Finally, the concluding remarks are given in Section 8.

2. Related work

In this section, we provide an overview for the research work related to the two major tasks, nucleus segmentation and HCC image classification, to be addressed in this paper.

2.1. Segmentation

The segmentation of nuclei/cells plays an important role in computer-aided analysis of pathological images by automating the process of delineating the positions and regions of nuclei/cells. Several methods of nuclei/cells segmentation have been reported in the literature. These methods can be classified into three categories: (1) the intensity-based approach, (2) the mathematical morphology-based approach, and (3) the deformable template approach.

Intensity-based approach is most common for separating foreground from background. This method is based on discontinuities in gray level intensity of pixels for identifying the boundaries of nuclei. Examples can be found in [16] and [17], where a new edge operator called Teager energy operator was defined in [16] to detect the boundaries of nuclei and a novel cell segmentation method was proposed in [17] by integrating edge detection, edge thinning, and edge linking steps based on directional information to segment cells more accurately. Another example of using intensity-based approach is thresholding. The gray level intensity of each pixel is compared to the threshold in order to determine if the pixel belongs to the object or background. The threshold may be obtained globally or locally from an image. Most of thresholding algorithms use adaptive and iterative method to find an optimal threshold for segmenting the suspected cancer cells from the complex background [18–21]. However, this approach is not applicable to nucleus segmentation because the gray level intensity of an HCC biopsy image varies not only on the boundaries of nuclei, but also within nuclei and throughout the background.

Mathematical morphology is a technique for processing geometrical structures based on set theory. It provides a powerful tool for extracting essential shape characteristics and eliminating irrelevant ones. Examples of this approach can be found in [22–24] for blood cell segmentation using morphological operators and in [25–27] for nuclei segmentation using marker-controlled watershed transform.

Deformable template approach delineates the contours of objects using closed parametric curves that can deform under the influence of internal and external forces. The internal force will keep the contour smooth during deformation and the external force will move the contour toward a target shape. To find the contour of an object in an image, a closed curve must be placed near the desired boundary and then start an iterative relaxation process. This approach is used in cell segmentation for handling noise and spurious edges [28,29]. Other examples of using this approach include active contour model [30–32] and level set analysis [33].

In order to perform nucleus segmentation for HCC biopsy images effectively, we must solve the following problems:

- *High complexity in HCC biopsy images:* An HCC biopsy image always consists of many different substances, and different grades of HCC have different patterns in biopsy images. Since the complex structures in HCC biopsy images will produce too many meaningless edges, the edge detection method and morphological watershed transform are not suitable to this case. The deformable template approach is not appropriate either because it is very difficult to define the templates for nuclei in HCC biopsy images.
- *Various gray level intensities on boundaries, inside, and outside of nuclei:* It is very difficult to determine the most appropriate focal distance so that all nuclei are well-focused under the microscope. Besides, not all parts of the same tissue are equally stained. Darker background regions may be misclassified as nuclei while lighter nuclear regions may be misclassified as background.
- *High density of nuclei in high degree of HCC malignancy:* The density of nuclei will increase for higher grades of HCC. The cells/nuclei will crowd the space and the boundaries of cells become too unclear to be well separated.

Based on the above analysis, we propose a hybrid approach with special techniques to solve the segmentation problem of HCC biopsy images. First, we propose a dual morphological grayscale reconstruction method to remove noise and accentuate the shapes of nuclei. Then, a marker-controlled watershed transform is performed for finding the edges of nuclei. Finally, we apply the snake method of the deformable model to generate smooth and accurate contours for nuclei.

2.2. Classification

In this paper, we use three classifiers, k -nearest neighbor (k -NN), support vector machine (SVM), and SVM-based decision-graph classifiers, to grade HCC biopsy images. The k -NN classifier is well-known among all nonparametric classifiers. The k -nearest-neighbor decision rule classifies an observation by assigning it the label which is most frequently represented among the k -nearest neighbors. A decision is made by examining all the labels on the k -nearest neighbors and taking a vote. The operation of a k -NN classifier can be summarized by the following three basic steps [34]:

- (1) compute the distances between the new sample and all previous samples already classified into clusters;

- (2) sort the distances in increasing order and select k samples with the smallest distance values; and
- (3) apply the voting principle: a new sample is added (classified) to the cluster with the highest votes from k selected samples.

The second classification technique used in this paper for grading HCC biopsy images is the SVM method [35,36]. Compared with traditional classification methods which minimize the empirical training error, the goal of SVM is to minimize the upper bound of the generalization error by finding the largest margin between the separating hyperplane and the data. The theory of non-linear SVM is briefly described as follows.

Consider a training set of N samples in binary classification. Each sample is denoted by a tuple (\mathbf{x}_i, y_i) , where $\mathbf{x}_i = (x_{i1}, x_{i2}, \dots, x_{id})^T$ corresponds to the feature vector for the i th sample ($i = 1, 2, \dots, N$) in d -dimensional space and $y_i \in \{-1, 1\}$ denotes its two-class label. Any point \mathbf{x} on the hyperplane must satisfy the decision boundary $\mathbf{w} \cdot \mathbf{x} + b = 0$, where parameter \mathbf{w} is normal to the hyperplane. In practicality, a non-linear SVM is more widely used for the general case due to its non-linear mechanism that can effectively classify data which are non-separable by a linear SVM. A non-linear SVM can be formulated by the following optimization problem:

$$\min_{\mathbf{w}, b, \xi} \frac{1}{2} \|\mathbf{w}\|^2 + C \sum_{i=1}^N \xi_i$$

Subject to $y_i(\mathbf{w} \cdot \Phi(\mathbf{x}_i) + b) \geq 1 - \xi_i, \xi_i \geq 0, i = 1, 2, \dots, N$ (1)

where notation $\|\cdot\|$ represents the norm of a vector. In the above objective function, a training data \mathbf{x}_i is mapped to a higher dimensional space by a kernel function Φ , and penalty C is a user-specified parameter. By minimizing $(1/2) \|\mathbf{w}\|^2$, we can get the maximum margin between the separating hyperplane and the data. To reduce the number of training errors in linearly non-separable case, the penalty term $C \sum_{i=1}^N \xi_i$ consists of a number of positive-valued slack variables ξ_i which can be used to construct a soft margin hyperplane. Then, a test sample \mathbf{z} can be classified according to the following equation:

$$f(\mathbf{z}) = \text{sign}(\mathbf{w} \cdot \Phi(\mathbf{z}) + b) = \text{sign}\left(\sum_{i=1}^N \alpha_i y_i \Phi(\mathbf{x}_i) \cdot \Phi(\mathbf{z}) + b\right) \quad (2)$$

The test sample \mathbf{z} is classified to the positive class if $f(\mathbf{z}) = +1$, and is classified to the negative class if $f(\mathbf{z}) = -1$. In the above decision boundary equation, the parameters α_i are Lagrange multipliers which can be obtained by using quadratic programming [37].

The computation of $\Phi(\mathbf{x}_i) \cdot \Phi(\mathbf{x}_j)$, i.e. the dot product between pairs of vectors in the transformed space, is quite cumbersome and may suffer from the curse of dimensionality problem [37]. Since a kernel function K can be expressed as $K(\mathbf{x}_i, \mathbf{x}_j) = \Phi(\mathbf{x}_i) \cdot \Phi(\mathbf{x}_j)$ according to Mercer's theorem [37], the decision function of a non-linear SVM can be written as

$$f(\mathbf{z}) = \text{sign}\left(\sum_{i=1}^N \alpha_i y_i K(\mathbf{x}_i, \mathbf{z}) + b\right) \quad (3)$$

We choose radial basis function (RBF) as the kernel function for SVM due to the following reasons: (1) RBF kernel can handle the case where the data are not linearly separable. Besides, linear kernel is a special case of RBF kernel with specific parameters (C, γ) [38]. (2) Compared with polynomial and sigmoid kernels, RBF kernel has fewer parameters which need to be determined. (3) Sigmoid kernel is not valid under some parameters [36].

3. Image acquisition and enhancement

In this study, every image was obtained by taking the same acquisition and processing steps. Tissue was embedded in paraffin cubes after chemical processing and then cut into very thin sections. These sections were placed on glass slides and stained with colored dyes using hematoxylin and eosin technique. The images were acquired by a set of equipments including a high quality optical microscope, a high resolution CCD camera, and an image acquisition computer system. Each image was taken through a microscope with magnifying factor of 400. There were 804 images with size of 4000 by 3000 pixels captured by the above procedure. These images were analyzed by a group of experienced pathologists in Taichung Veterans General Hospital of Taiwan and classified into five grades (0–4) in advance for later comparison.

According to the characteristics for identifying HCC, the major features used for HCC grading are mainly related to nuclei; therefore, it is essential to segment nuclei from background of the image correctly. An HCC biopsy image may contain many undesirable elements such as erythrocyte, leukocyte, and impurities as shown in Fig. 1. Since nuclei/cells may be located in the upper or lower position of the tissue, not all nuclei/cells are focused very well at the same time. Moreover, nuclei and cytoplasm are not always transparent and the intensities in them are not always uniform. Therefore, if a segmentation method is directly applied to an HCC biopsy image without preprocessing, it will generate inaccurate edges for nuclei. To solve this problem, we propose a dual morphological grayscale reconstruction method to eliminate irrelevancies while preserving the shapes of nuclei in biopsy images.

Morphological grayscale reconstruction was originally proposed in [39,40] for image analysis. The first stage of our dual morphological grayscale reconstruction method is the same as a regular grayscale morphological reconstruction algorithm, which starts with eroding the original image by an appropriate structuring element. The eroded image and original image are considered as the marker and the mask images, respectively. Then, a series of conditional dilations are applied to the marker image by using an elementary isotropic structuring element with the original image as the mask image. In the second stage, the resultant image obtained from the first stage will be dilated by an appropriate structuring element to produce a marker image and the image before dilating is treated as the mask image. Then, a series of conditional erosions are applied to the marker image by using an elementary isotropic structuring element with the image generated from the first stage as the mask image. A diagram depicting the execution flow of dual morphological grayscale reconstruction method is shown in Fig. 2. In removing small

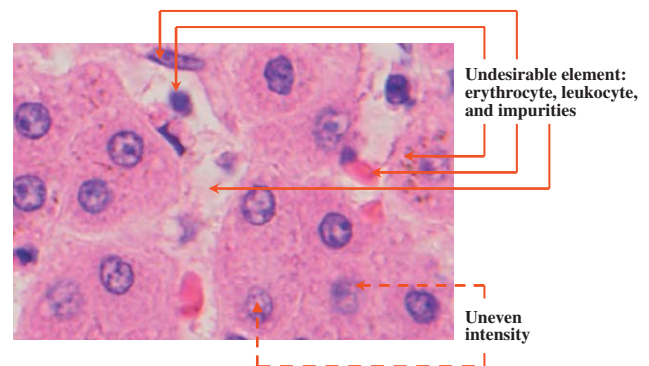


Fig. 1. An HCC biopsy image may contain many undesirable elements such as erythrocyte, leukocyte, and impurities.

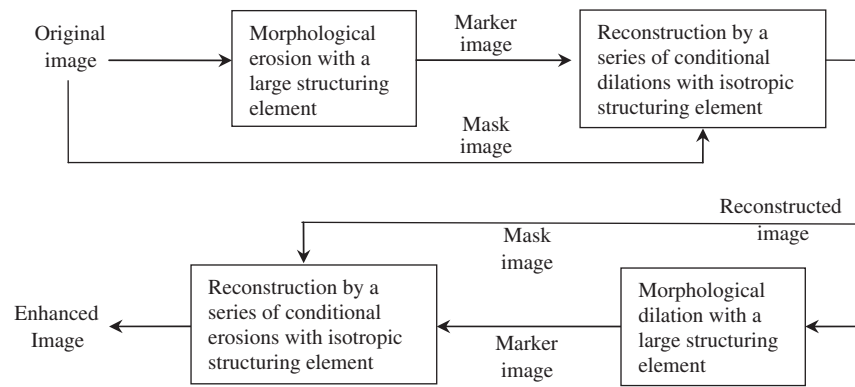


Fig. 2. The flowchart of dual morphological grayscale reconstruction method.

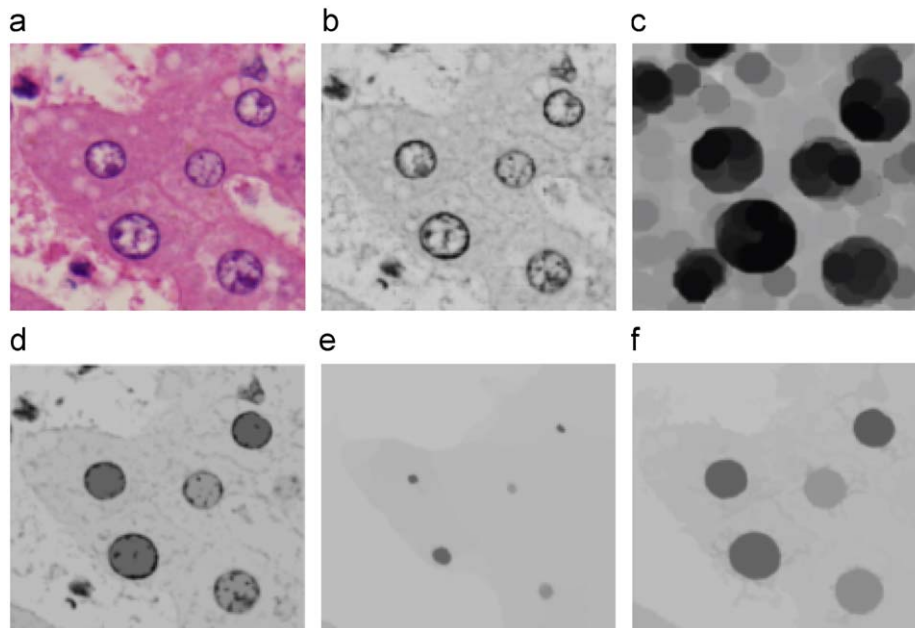


Fig. 3. An example of dual morphological grayscale reconstruction for HCC biopsy images. (a) The original RGB color image. (b) The grayscale image obtained from red plane. (c) Eroded image of (b). (d) Morphological reconstruction result using (b) and (c) as the mask and marker images, respectively. (e) Dilated image of (d). (f) Final enhanced result after morphological reconstruction using (d) and (e) as the mask and marker images, respectively (For interpretation of the references to color in this figure legend, the reader is referred to the web version of this article.).

blemishes, the dual morphological grayscale reconstruction algorithm is more effective than conventional morphological grayscale operations in terms of preserving the overall shapes of objects.

An example to illustrate the process of enhancement for an HCC biopsy image is shown in Fig. 3. For convenience of illustration, we only show a subpart of a biopsy image. Fig. 3(a) is the original RGB color image. Fig. 3(b) is the grayscale image in the red plane. Fig. 3(c) is obtained by eroding from Fig. 3(b) with a disk shape structuring element of radius 20. Fig. 3(d) is the result from morphological reconstruction using Figs. 3(b) and (c) as the mask and marker images, respectively. Fig. 3(e) is obtained by dilating from Fig. 3(d) with a disk shape structuring element of radius 20. Then, a dilation followed by a series of erosions is applied by using Fig. 3(d) as the mask image and Fig. 3(e) as the marker image. The final result is shown in Fig. 3(f). To further illustrates the concept of dual morphological grayscale reconstruction method, let us look at the profiles shown in Fig. 4 which indicate the intensity levels of pixels along row 178 of the images in Figs. 3(b)–(f). Fig. 4(a) shows the erosion result of

the intensity diagram of row 178 in Fig. 3(b) using a disk shape structuring element of radius 20. Fig. 4(b) is the result of performing a series of conditional dilations on the intensity diagram of Fig. 3(c) using an isotropic structuring element of radius 1. Fig. 4(c) shows the dilation result from the intensity diagram of Fig. 3(d) using a disk shape structuring element of radius 20. Fig. 4(d) is the result of performing a series of conditional erosions on the intensity diagram of Fig. 3(e) using an isotropic structuring element of radius 1. The above process is performed row-by-row and the final result of the dual morphological grayscale reconstruction method is shown in Fig. 3(f). As we can see that the shapes of nuclei in Fig. 3(f) are well preserved and other irrelevant objects are removed.

4. Segmentation of nuclei

The most important task in this research is to segment the nuclei and extract features from them for HCC grading. In order to accurately segment the nuclei, we first apply a marker-controlled

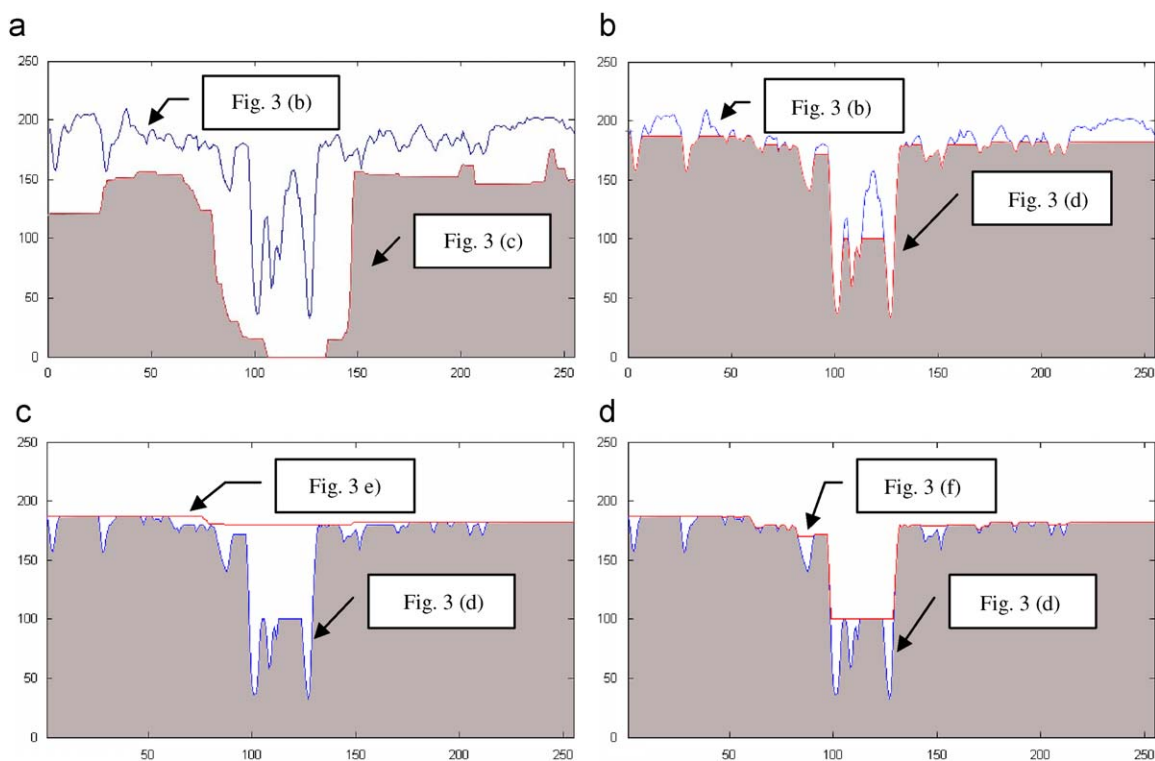


Fig. 4. Morphological grayscale reconstruction using row 178 of Fig. 3(b–f) as the example.

watershed transform [41,42] to detect the possible edges of nuclei, then use a set of heuristic rules provided by experienced physicians to remove the unlikely edges, and finally apply the gradient vector flow (GVF) method [32,43–45] for refining the contours of nuclei.

The basic idea of watershed transform is to regard a grayscale image as a topographic relief, which is flooded starting at surface global minima with water. The water level would increase to fill up lower elevation points first. When water coming from different basins would meet, dams called watershed ridge lines are built. However, applying watershed transform to HCC biopsy images always leads to over-segmentation due to noise or other local irregularities of the gradient [41]. In this paper, we use marker-controlled watershed transform [46] to solve the over-segmentation problem. First, a set of foreground markers deeper than their immediate surroundings are generated by finding the regional minima in the image. This ensures that each nucleus will contain a foreground marker. Then, background markers are found as the watershed ridge lines by computing the watershed transform of the distance transform [41] of the black-and-white image containing foreground markers. Finally, the gradient magnitude image obtained from traditional watershed transform is modified so that its regional maxima only occur at foreground and background markers pixels.

An example of marker-controlled watershed transform is presented in Fig. 5. Fig. 5(a) is an enhanced image obtained from the preprocessing step as described in Section 3. Fig. 5(b) shows over-segmented result generated from the conventional watershed transform without using markers. Foreground markers, with each one inside a nucleus, are generated by computing the regional minima as shown in Fig. 5(c). Background markers are shown in Fig. 5(d). Fig. 5(e) shows the watershed ridge lines with no over-segmentation effect when applying the marker-controlled watershed transform. Then, we use Fig. 5(e) to coincide with the original image of the same size (similar to Fig. 1) and apply a set of heuristic rules provided by

experienced physicians to remove erythrocyte (in fresh red color), leukocyte (in deep color), fat (in white color), incomplete shapes (at the margin of the image), and shapes with rough edges. The final segmentation result is shown in Fig. 5(f).

In our HCC grading system, information about the shape of nucleus plays an important role in classification. The contours of nuclei obtained from the above process seem not seamless enough to the correct shapes of nuclei. Therefore, to get smoother and more accurate contours of nuclei, the gradient vector flow (GVF) method [45], which uses a new type of external force for active contours (snakes), is applied to refine the contour of nucleus. We use the contour obtained from the previous segmentation result as the initial contour, and then move this contour close to the more accurate nuclear contour under the influence of internal forces depending on the intrinsic properties of the curve and external forces derived from the image data. The images in Fig. 6 are of size 175×225 pixels and directly clipped from a biopsy image. Fig. 6(a) is an example of nuclear contours obtained from marker-controlled watershed transform, and Fig. 6(b) shows the refined nuclear contours after applying the GVF method. Two other examples of contour-finding results are also shown in Fig. 7. The original size of Fig. 7(a) is 1000×1000 pixels. This image is cut from an original biopsy image of size 4000×3000 pixels and then reduced to the size of 256×256 pixels for displaying. The original size of Fig. 7(b) is 2800×2750 pixels and also reduced to the size of 256×256 pixels for displaying.

5. Feature extraction

The criteria of HCC grading are usually based on the following five types of characteristics: *nuclear size*, *nucleocytoplasmic ratio*, *nuclear irregularity*, *hyperchromatism*, and *anisonucleosis*. According to these characteristics, HCC can be classified into five grades (0–4) [47,48]. Grade 0 stands for normal situation and the grade

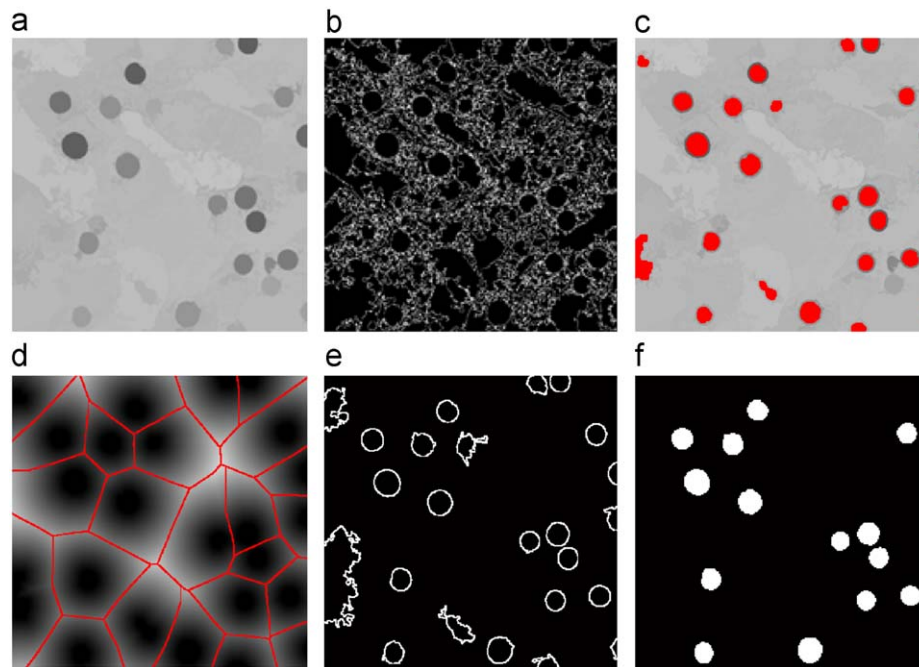


Fig. 5. An example of nuclei segmentation by using marker-controlled watershed transform. (a) Image obtained from preprocessing step. (b) Ridge lines obtained from regular watershed transform. Over-segmentation problem occurs. (c) Foreground markers associated with nuclei. (d) Background markers are indicated by ridge lines. (e) Ridge lines obtained from marker-controlled watershed transform. (f) Segmentation result after removing undesirable elements by using heuristic rules.

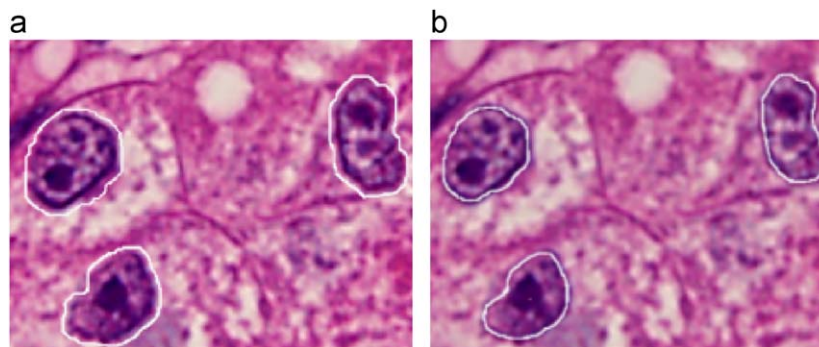


Fig. 6. An example of refining contours of nuclei by using GVF active contour method. (a) Original contours of nuclei generated from watershed transform. (b) Refined contours of nuclei after applying the GVF active contour method.

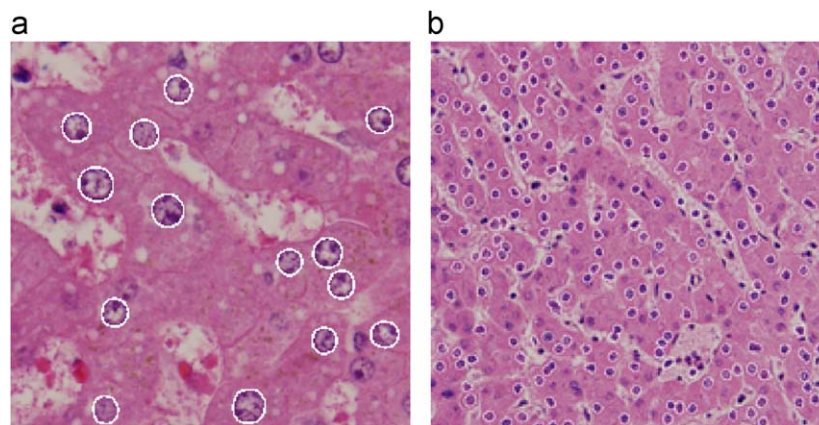


Fig. 7. Two examples of segmentation results for biopsy images. The original size of (a) is 1000×1000 pixels and the original size of (b) is 2800×2750 pixels. Both images are shrunk to 256×256 pixels for convenience of displaying.

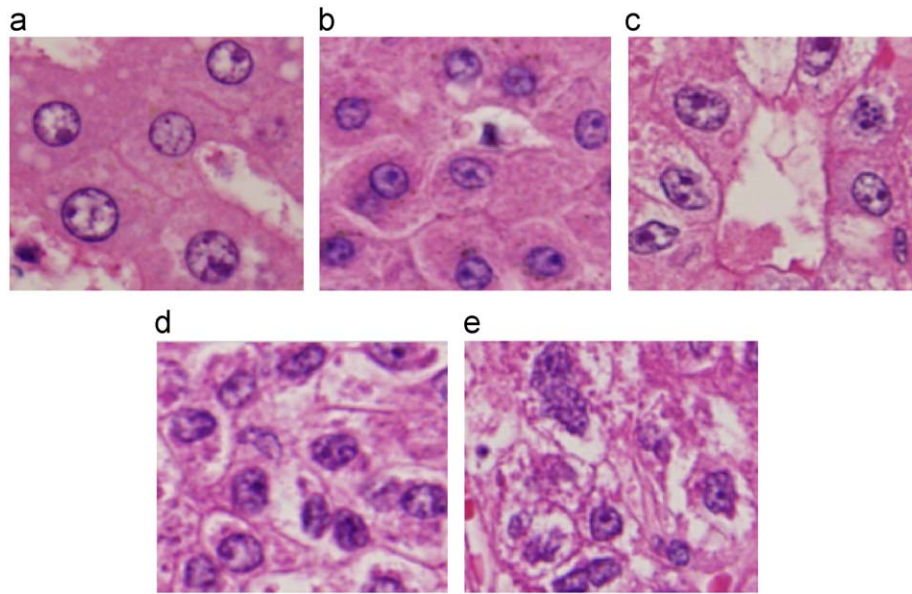


Fig. 8. Examples of HCC biopsy images in different grades (subparts cut from the original images of size 4000×3000 pixels). (a) Normal HCC. (b) Grade 1 HCC. (c) Grade 2 HCC. (d) Grade 3 HCC. (e) Grade 4 HCC.

Table 1
Five types of characteristics for HCC grading.

Type	Grade 0	Grade 1	Grade 2	Grade 3	Grade 4
Nuclear size	Smaller	Small	Medium	Medium	Large
N/C ratio	Lower	Low	Medium	High	High
Irregularity	Lower	Low	Medium	High	High
Hyperchromatism	Lower	Low	Medium	High	High
Anisonucleosis	Low	Low	Low	Medium	High

number will increase with increasing malignancy level. Some examples of biopsy images with five different grades are shown in Fig. 8. The HCC biopsy images of lower grades have much more abundant cytoplasm, more transparent nuclei, and less nuclear irregularity in contrast to the HCC biopsy images of higher grades. Table 1 shows the summary of the variations among different grades of HCC images based on these five types of characteristics.

The above five types of characteristics are provided by experienced pathologists and usually used for HCC grading. In addition, to facilitate computer processing and image analysis, the pathologists also suggest *nuclear texture* as the sixth type of characteristics. Then, 14 features based on these six types of characteristics are extracted from HCC biopsy images for classification. For convenience of explanation, we introduce the following notations in feature representation:

- n : total number of nuclei in the image,
- N_i : the i th nucleus in the image, $1 \leq i \leq n$,
- T : the minimum spanning tree covering all N_i in the image,
- $w(N_i, N_j)$: the distance in terms of number of pixels between the centroid of N_i and N_j ,
- $\|N_i\|$: size of nucleus N_i (i.e. number of pixels in N_i),
- $\|C_i\|$: size of cytoplasm of nucleus N_i (i.e. number of pixels in C_i),
- $\Gamma(N_i)$: circumference of nucleus N_i ,
- $N_i(x, y)$: the gray-value of the pixel at location (x, y) in nucleus N_i ,
- $B(N_i)$: the overall size of all bright-spots in nucleus N_i ,
- $D(N_i)$: the overall size of all dark-spots in nucleus N_i , and
- $Z_{d\theta}^i$: the gray-level co-occurrence matrix for the neighboring pixels in N_i separated by a distance d in direction θ .

Now, we are ready to present the 14 features derived from the six types of characteristics for HCC grading as follows.

5.1. Type-1: nucleocytoplasmic ratio

Biopsy images with high HCC grades usually have high degree of clustering among neighboring nuclei, high nucleus-to-cytoplasm ratio, and small cell-size. Since the cells are usually congested together and the nuclei may cluster in arbitrary shapes, it is very difficult to identify the boundaries of cells especially for the cases of higher HCC grades. As a result, there is no straightforward method to measure the areas of cells or cytoplasm. To tackle this problem, we apply a minimum spanning tree (MST) model [15] as follows.

First, we envision a segmented biopsy image as a complete connected weighted graph, in which nodes are the nuclei and the weight associated with an edge is the distance between the centroid of two nuclei. Then, a minimum spanning tree T can be found from this connected complete graph for extracting the three type-1 features. Fig. 9(b) shows an example of the MST generated from Fig. 9(a). In this minimum spanning tree model, we use the inverse of mean distance between any two nearest neighboring nuclei in T to represent the degree of clustering among a group of nuclei. Since the boundaries of nuclei are detectable, it is not difficult to find the sizes of nuclei. However, the boundaries of cells are not so obvious. Thus, we need a special method to estimate the size of cytoplasm and subsequently the size of cells.

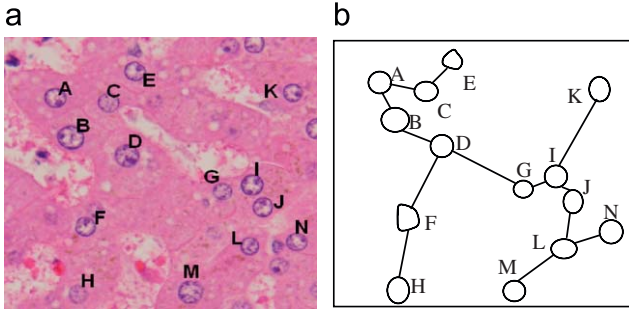


Fig. 9. An example of minimum spanning tree constructed from a segmented HCC biopsy image. (a) Original HCC biopsy image. (b) A MST constructed from (a). Each nucleus is connected with its nearest neighboring nucleus.

To estimate the size of cytoplasm C_a of a given nucleus N_a , we propose a novel heuristic method based on MST described as follows:

- (1) Find the set S of all nuclei neighboring to N_a in minimum spanning tree T .
- (2) For each nucleus $N_j \in S$, dilate the boundaries of N_j and N_a outwards simultaneously and one pixel at a time until the two boundaries meet together. Then, calculate the size (in terms of number of pixels) of the area A_j^a between the starting and stopping boundaries of N_a .
- (3) Find the average size μ of all areas A_j^a

$$\left(\text{i.e. } \mu = \frac{1}{|S|} \sum_{j=1}^{|S|} \|A_j^a\| \right),$$

and μ is the estimated size of cytoplasm C_a of nucleus N_a ($\|C_a\| = \mu$).

Once a minimum spanning tree is constructed, we can obtain sizes of cells, nuclei, and cytoplasm and subsequently define three type-1 features using the following formulas:

- *Degree of clustering among neighboring nuclei*

$$f_1 = \frac{1}{n-1} \left(\sum_{(N_i, N_j) \in T} (w(N_i, N_j))^{-1} \right) \quad (4)$$

- *Mean nucleus-to-cytoplasm ratio*

$$f_2 = \frac{1}{n} \sum_{i=1}^n (\|N_i\| / \|C_i\|) \quad (5)$$

- *Mean cell size*

$$f_3 = \frac{1}{n} \sum_{i=1}^n (\|N_i\| + \|C_i\|) \quad (6)$$

5.2. Type-2: nuclear irregularity

The shapes of nuclei are no longer kept round in cancerous tissues because of their serious deformity. For better capturing the shape information, we use both region-based and contour-based methods to extract anti-circularity, area irregularity, and contour irregularity of nuclei as the three shape features to reflect the irregularity of nuclei in biopsy images.

- *Mean anti-circularity of nuclei (contour-based)*

$$f_4 = \frac{1}{n} \sum_{i=1}^n \left(\frac{\Gamma^2(N_i)}{4\pi\|N_i\|} \right) \quad (7)$$

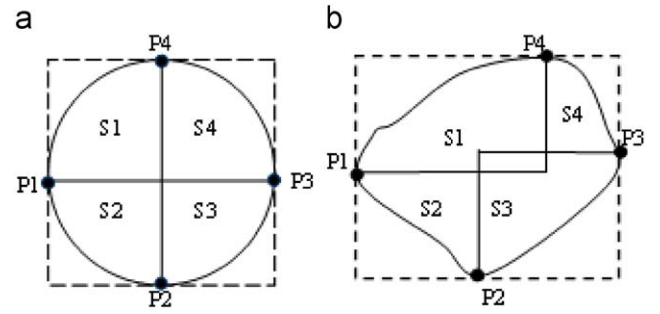


Fig. 10. Two examples of area irregularity. (a) A round nucleus. (b) An irregular nucleus.

- *Mean area irregularity of nuclei (region-based):* One way to explore irregularity of nuclei is to evaluate their asymmetric properties. To achieve this goal, we propose the following novel method. First, a nucleus is rotated so that its major axis becomes horizontal. Then, the rotated nucleus is enclosed by a minimum bounding rectangle (MBR). There is at least one intersecting point between a nucleus and each side of its MBR as shown in Fig. 10. If there are two or more intersecting points at one side, the middle one is selected as the representative intersecting point. Then, a nucleus is partitioned into four parts as follows. If an intersecting point is on a vertical side of the MBR, a horizontal cutting line will go through this point. If an intersecting point is on a horizontal side of the MBR, a vertical cutting line will go through this point. Consequently, four possibly overlapping areas S1, S2, S3, and S4 will be formed with each area surrounded by a segment of nucleus's boundary, a vertical line, and a horizontal line. Fig. 10 shows two examples of nucleus partition, where Fig. 10(a) is a benign nucleus which has low area irregularity while Fig. 10(b) is a malignant nucleus which has higher area irregularity. Then, area irregularity of nucleus can be estimated by the following formula:

$$f_5 = \frac{1}{n} \sum_{i=1}^n \left(\frac{1}{4} \sum_{j=1}^4 \max_{k=1, \dots, 4, k \neq j} |(\|S_j^i\| - \|S_k^i\|)| \right) \quad (8)$$

- *Mean contour irregularity of nuclei (contour-based):* The contour of a nuclear shape can be represented by a sequence of k equal spacing sample boundary points $\{p_0, p_1, p_2, \dots, p_{j-1}, p_j, \dots, p_{k-1}\}$ with $p_k = p_0$ and $p_{-1} = p_{k-1}$. Let $p_j(w)$ be the boundary point with a distance of w pixels from the current point p_j . Let x_j and y_j be the x - and y -coordinate of point p_j , and $x_j(w)$ and $y_j(w)$ be the x - and y -coordinate of point $p_j(w)$. The tangents at point p_j and p_{j-1} can be approximated by $\overline{p_j p_j(w)}$ and $\overline{p_{j-1} p_{j-1}(w)}$, respectively. Since a curvature function is a function of angular changes of a boundary tangent, curvature at a boundary point p_j can be expressed as a differentiation of successive tangent values calculated in window w [49] as expressed in Eq. (9) and shown in Fig. 11.

$$d_j^i = \tan^{-1} \frac{y_j - y_j(w)}{x_j - x_j(w)} - \tan^{-1} \frac{y_{j-1} - y_{j-1}(w)}{x_{j-1} - x_{j-1}(w)}, d_{-1}^i = d_{k-1}^i \quad (9)$$

Then, we can define contour irregularity of a nucleus as the averaging differentiation of all successive tangent values and the mean contour irregularity (f_6) as the averaging contour irregularity for all nuclei.

$$f_6 = \frac{1}{n} \sum_{i=1}^n \frac{1}{k} \left(\sum_{j=0}^{k-1} |d_j^i - d_{j-1}^i| \right) \quad (10)$$

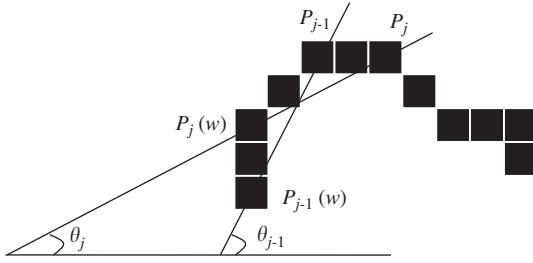


Fig. 11. An example of measuring curvature at boundary point p_j of a nucleus with partial enlargement. The tangents at boundary points p_j and p_{j-1} can be approximated by $p_j p_j(w)$ and $p_{j-1} p_{j-1}(w)$, respectively. Tangent values at points p_j and p_{j-1} are θ_j and θ_{j-1} , respectively. A curvature function is a function of angular changes of a boundary tangent. Thus, curvature at boundary point p_j can be estimated by $\theta_j - \theta_{j-1}$. In this example, sample spacing is two pixels and window distance w is four pixels.

5.3. Type-3: hyperchromatism

Hyperchromatism represents excessive pigmentation in hemoglobin content of erythrocytes. It is an important characteristic appearing in a malignant tumor. For the case of higher grade HCC, chromatin abnormality will result in increasing staining capacity of nuclei. Thus, the intensity of nucleus in higher HCC grade usually appears darker than that of normal nucleus. Also, within a malignant tumor, increasing chromatin will cause more holes within nuclei to occur in HCC biopsy images. The holes are reflected by the ratio of bright and dark spots in nucleus. In our system, the bright and dark spots can be detected by top-hat and bottom-hat transforms [41,50], respectively, on nuclei using a disk shape structuring element of radius 5. Top-hat transform is the difference between an input image and its opening by some structuring element, and bottom-hat transform is the difference between the closing and the input image. Top-hat transform returns an image containing elements that are smaller than the structuring element and brighter than their surroundings. Bottom-hat transform returns an image containing elements that are smaller than the structuring elements and darker than their surroundings. By using top- and bottom-hat transforms, the bright and dark spots in nucleus can be easily identified. Based on the above discussion, we define two type-3 features related to hyperchromatism as follows:

- Mean intensity of nuclei

$$f_7 = \frac{1}{n} \sum_{i=1}^n \left(\frac{1}{\|N_i\|} \sum_{\forall (x,y) \in N_i} N_i(x,y) \right) \quad (11)$$

- Mean spot-areas ratio in nuclei

$$f_8 = \frac{1}{n} \sum_{i=1}^n \left(\frac{1}{\|N_i\|} (\|B(N_i)\| + \|D(N_i)\|) \right) \quad (12)$$

5.4. Type-4: mean nuclear size

HCC with higher grade implies higher probability of larger nuclei. Therefore, the average size of nucleus can be used as a criterion for HCC grading.

- Mean nuclear size

$$f_9 = \frac{1}{n} \sum_{i=1}^n \|N_i\| \quad (13)$$

5.5. Type-5: anisonucleosis

In the cases with high HCC grades, the variance among the areas of nuclei is noticeable. Thus, the following two features can be derived from size distribution of nuclei for identifying HCC with high grades.

- Standard deviation of nuclear size: This feature is calculated by the square root of the average squared deviation from the mean nuclear size.

$$f_{10} = \left(\frac{1}{n} \sum_{i=1}^n (\|N_i\| - f_9)^2 \right)^{1/2} \quad (14)$$

- Extreme nuclear size difference: Sometimes in grade-4 HCC images, there are only a few nuclei having large area differences. So feature f_{10} (standard deviation of nuclear size) cannot represent anisonucleosis effectively. In this case, we use the difference between maximal and minimal size of nucleus to measure anisonucleosis.

$$f_{11} = \max_{i=1 \dots n} \{\|N_i\|\} - \min_{i=1 \dots n} \{\|N_i\|\} \quad (15)$$

5.6. Type-6: nuclear texture

Gray level co-occurrence matrix (GLCM) has been shown to be very useful for texture analysis [51–54]. For nuclear texture analysis, the following three features are derived from GLCM $Z_{d\theta}^i$ associated with nucleus N_i , where neighboring pixels are separated by a distance d in direction θ . In our implementation, we chose $d=1$ and $\theta=0^\circ, 45^\circ, 90^\circ, 135^\circ$.

- Mean energy in nuclei

$$f_{12} = \frac{1}{n} \sum_{i=1}^n \sum_{j,k} (Z_{d\theta}^i[j,k])^2 \quad (16)$$

- Mean contrast in nuclei

$$f_{13} = \frac{1}{n} \sum_{i=1}^n \sum_{j,k} (j-k)^2 Z_{d\theta}^i[j,k] \quad (17)$$

- Mean homogeneity in nuclei

$$f_{14} = \frac{1}{n} \sum_{i=1}^n \sum_{j,k} \frac{Z_{d\theta}^i[j,k]}{1+|j-k|} \quad (18)$$

6. Classification of HCC biopsy images

The performance of our automatic HCC grading system in this study is evaluated by three classifiers: the k -NN classifier, the support vector machine (SVM) classifier, and the SVM-based decision-graph classifier.

Support vector machine is a popular classification and regression technique [35,55]. The basic idea of SVM is to transform data into a higher dimensional space and find the optimal hyperplane with maximal separation margin between two classes. In our HCC grading system, there are five classes (G_0 – G_4) to be considered. How to effectively classify multi-classes is still an on-going research issue [56,57]. Several methods have been proposed by combining binary SVM classifiers for solving this problem. The two commonly used approaches are “one-against-all” and “one-against-one.” The former constructs k SVM models within k classes and separates each class from all others while the latter constructs $k(k-1)/2$ SVM models between any

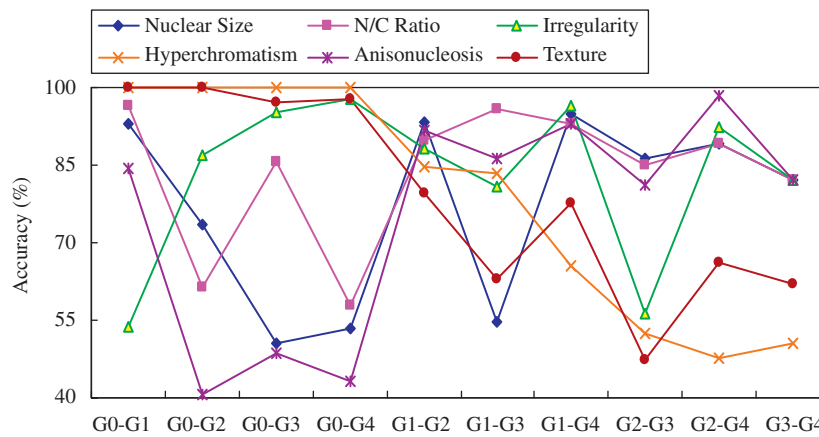


Fig. 12. Accuracy of classification using only one of the six types of features for distinguishing any two HCC grades by SVM.

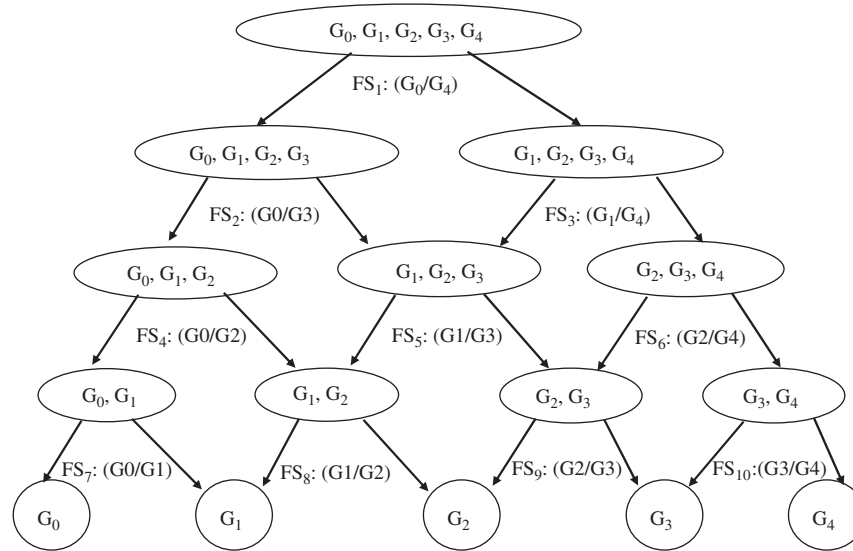


Fig. 13. The SVM-based decision-graph classifier for HCC grading.

pair of classes and separates all classes pair-wise. In this study, the implementation of SVM used in our experiment is LIBSVM [58] which utilizes “one-against-one” approach for multi-class classification. We select radial basis function (RBF) as the kernel function and use cross validation process to decide penalty parameter of C-SVC (C-support vector classification).

Conventional image classifying methods use a fixed number of image features for classification. However, in HCC grading, a different feature set must be used in order to distinguish a different pair of grades effectively. For example, hyperchromatism and nuclear texture are the two best types of features if we want to distinguish grade 0 (G_0) from grade 1 (G_1) while nucleocytoplasmic (or N/C) ratio is the best if we want to distinguish grade 1 (G_1) from grade 3 (G_3) as shown in Fig. 12. In other words, there is no single type of features that can well distinguish all five grades. Furthermore, not all feature types are equally important for distinguishing any given pair of grades. Therefore, in order to achieve effective classification for HCC biopsy images, we propose “one-against-one” support vector classifier established upon a decision-graph model as shown in Fig. 13, where each decision node is associated with an optimal subset of features for differentiating two particular grades of images. In our

Table 2

Feature subsets and pairs of grades to be differentiated.

Pair of grades	Set of features used to distinguish the pair of grades
(G_0, G_4)	$FS_1 = \{f_3-f_5, f_7, f_8, f_{13}\}$
(G_0, G_3)	$FS_2 = \{f_1-f_5, f_7, f_8, f_{12}, f_{14}\}$
(G_1, G_4)	$FS_3 = \{f_3-f_5, f_8, f_9, f_{10}-f_{12}\}$
(G_0, G_2)	$FS_4 = \{f_1, f_2, f_4-f_8, f_{11}\}$
(G_1, G_3)	$FS_5 = \{f_1-f_5, f_{10}, f_{12}, f_{13}\}$
(G_2, G_4)	$FS_6 = \{f_2-f_5, f_7, f_8, f_{10}-f_{14}\}$
(G_0, G_1)	$FS_7 = \{f_2-f_4, f_6-f_9, f_{13}, f_{14}\}$
(G_1, G_2)	$FS_8 = \{f_5, f_7-f_{10}, f_{12}-f_{14}\}$
(G_2, G_3)	$FS_9 = \{f_1-f_4, f_6-f_9, f_{12}-f_{14}\}$
(G_3, G_4)	$FS_{10} = \{f_1-f_{14}\}$

SVM-based decision-graph classifier, the optimal subset of features at each decision node can be found by the feature selection method to be described next.

The two well-known feature selection methods, sequential forward selection (SFS) and sequential backward selection (SBS), are step-optimal only since the best (the worst) feature is always added (discarded) [59]. However, they all result in nested feature

subsets without any chance to correct the decision in later steps causing the performance to be often far from optimal. A more efficient method, called sequential floating forward selection (SFFS) [60], was designed by combining SFS and SBS to avoid the nesting effect. The basic idea of SFFS is based on the “plus l -take away r ” concept. It consists of applying l times SFS followed by r times SBS as long as the resulting subset is better than the previously evaluated ones at that level [59–61]. This method allows us to choose a subset of features so that the feature space is optimally reduced according to a certain evaluation criterion. The criterion used is the correct classification rate (CCR) evaluated by the classifier. It is worth noting that SFFS method performs almost as well as the branch-and-bound algorithm for optimal feature selection while demanding lower cost of computation [62].

The optimal feature subset associated with each node of the SVM-based decision-graph classifier in Fig. 13 is presented in Table 2. At each node, an optimal subset of features was selected from the 14 features so that the two extreme grades can be effectively distinguished by those selected features. For instance, the two extreme grades are G_0 and G_4 at the root node, which can be distinguished by the set of optimal features $FS_1 = \{f_3 - f_5, f_7, f_8, f_{13}\}$. The two extreme grades for the right child of the root node are G_1 and G_4 , which can be differentiated by the set of optimal features $FS_3 = \{f_3 - f_5, f_8, f_9, f_{10} - f_{12}\}$. Our SVM-based decision-graph classifier can prevent irrelevant or insignificant features from being selected and reduce the dimension of feature space at each decision node while avoiding possible interferences during the decision process.

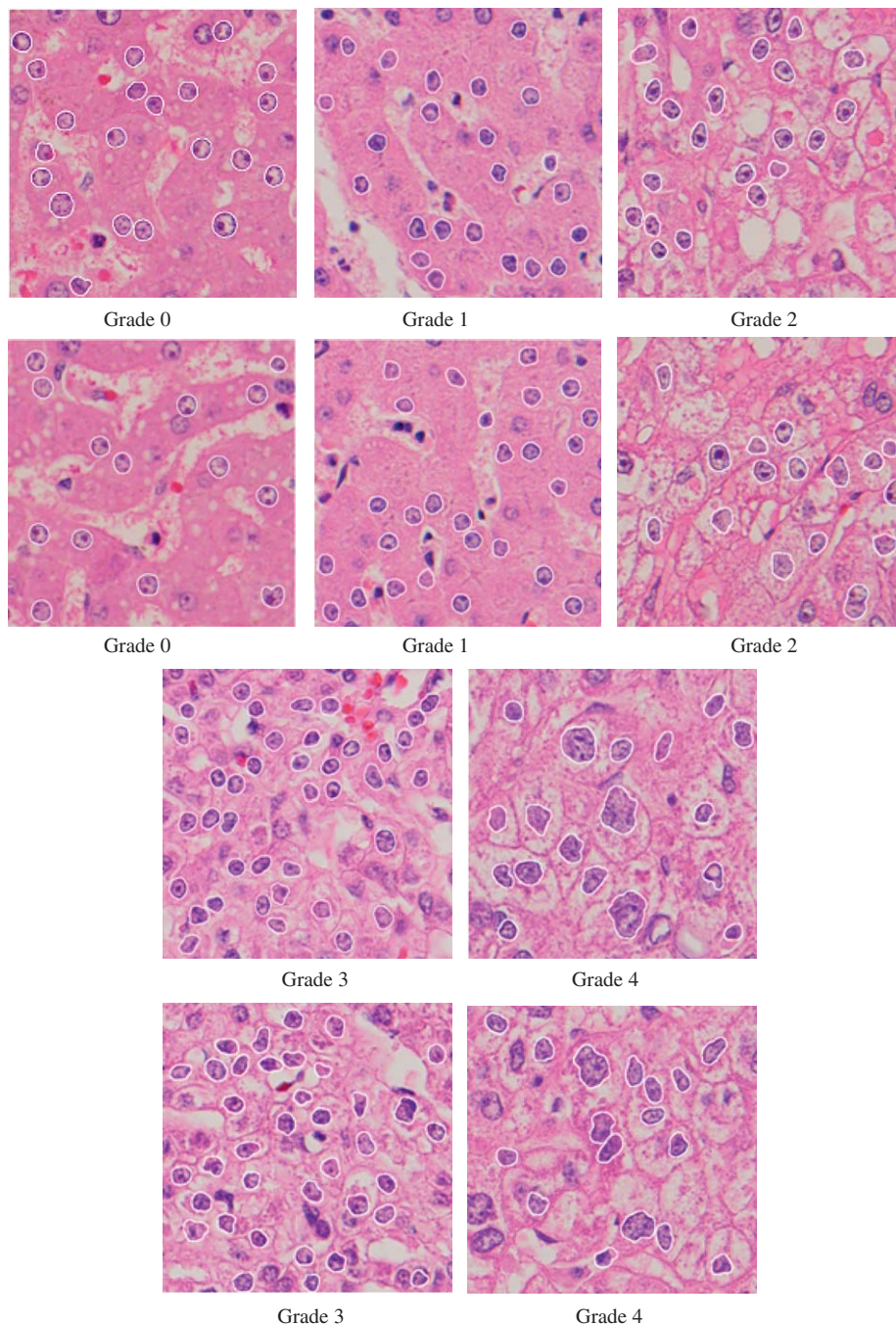


Fig. 14. Successful examples of segmentation for different HCC grades.

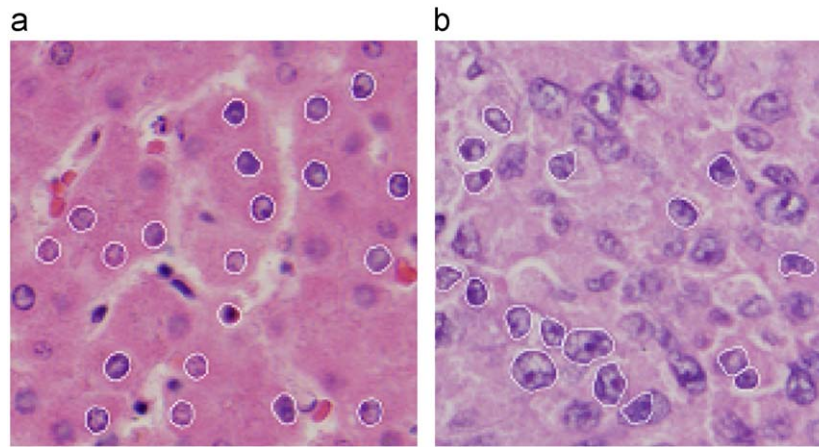


Fig. 15. Two failure examples of segmentation.

Table 3

The results of HCC classification by using SVM and only one type of features as the criteria for grading.

	Type-1	Type-2	Type-3	Type-4	Type-5	Type-6
Accuracy (%)	75.66	71.84	52.48	58.94	74.50	68.05

7. Experimental results

We have evaluated the performance of our HCC grading system using 804 biopsy images of size 3000×4000 pixels obtained from more than 100 patients. To establish the ground truth, biopsy images were commonly graded by a group of experienced pathologists of Taichung Veterans General Hospital in Taiwan. Before features extraction, nuclei segmentation must be performed. Fig. 14 shows 10 examples of successful nuclei segmentation in different grades. We also found some failure examples in nuclei segmentation. For example, some nuclei are not so well-focused in Fig. 15(a) and the stained color in nuclei is too light in Fig. 15(b).

To evaluate the performance of our HCC grading system, we used 200 images as the training samples and another 604 images for testing. Among the 604 testing samples, 58 images were graded as G_0 , 26 images were graded as G_1 , 75 images were graded as G_2 , 220 images were graded as G_3 , and 225 images were graded as G_4 by experienced pathologists. For easy processing, each image is divided into 12 non-overlapping equal parts of size 1000×1000 pixels. Therefore, 2400 sub-images were actually used for training and 7248 sub-images were used for testing. In HCC grading, if there is more than one grade appearing in different sub-images of the same original image in the result of classification, the highest grade is regarded as the grade of the original image.

First, we try to examine the accuracy of support vector classification by using only one of the six types of features and the results are presented in Table 3. As we can see that type-1 features (degree of clustering among neighboring nuclei, nucleus-to-cytoplasm ratio, and cell-size) can achieve 75.66% of accuracy, and type-5 features (standard deviation of nuclear size and extreme size difference between nuclei) can achieve 74.5% of accuracy. All other four types of features have worse classification results if they are used individually as the criteria for grading. This verifies the conjecture that every type of features is useful for

classification and multiple types of features are required to achieve high accuracy of HCC grading.

The second experiment is to examine the performance of SVM classification by using all 14 features derived from the six feature types and the result is presented in Table 4, where the overall accuracy rate of classification is 92.88%. Note that grade 0 (normal) and grade 1 are 100% accurate. This implies that benignancy is never misclassified as malignancy and vice versa. The performance is degraded in grading the case of grade 3, where only 89.55% of accuracy is achieved. Such a result is reasonable even for experienced pathologists, because it is very likely to misclassified grade 3 as grade 2 or grade 4.

The third experiment is to examine the performance of our SVM-based decision-graph classifier with selected features at each decision node and the result is presented in Table 5. As we can see that our SVM-based decision-graph classifier has 100% of accuracy in grading G_0 and G_1 . The lowest accuracy is 91.36% in grading G_3 . This result seems that our method is more “aggressive” as compared to manual grading because 18 out of 220 images were classified as G_4 instead of G_3 . On an average, the overall accuracy is 94.54%, which is 1.66% higher than the SVM classifier by using all 14 features. Therefore, the performance of our SVM-based decision-graph classifier with feature selection at each decision node is better than the performance of SVM classifier without feature selection. This result confirms our previous assertion that some features suitable for differentiating a given pair of grades may interfere with other features suitable for differentiating other pair of grades in grading HCC biopsy images.

The fourth experiment is to examine the performance of HCC classification by using k -NN classifier and all 14 features. We use the same sets of images for training and testing as in the previous two experiments. The accuracy of k -NN classification can achieve up to 90.07% if $k=3$ as presented in Table 6. In summary, our SVM-based decision-graph classifier has better performance than the SVM classifier, which in turn has better performance than the k -NN classifier.

Table 4

The performance of HCC classification by using SVM and all 14 features.

Grades	Visual grading	Classification result					Accuracy (%)
		G_0	G_1	G_2	G_3	G_4	
G_0	58	58	0	0	0	0	100
G_1	26	0	26	0	0	0	100
G_2	75	0	0	70	3	2	93.33
G_3	220	0	2	2	197	19	89.55
G_4	225	0	0	8	7	210	93.33
Total	604	58	28	80	207	231	92.88

Table 5

The performance of HCC classification by using our decision-graph SVM classifier with an optimal subset of features selected by SFFS method at each decision node.

Grades	Visual grading	Classification result					Accuracy (%)
		G_0	G_1	G_2	G_3	G_4	
G_0	58	58	0	0	0	0	100
G_1	26	0	26	0	0	0	100
G_2	75	0	0	72	2	1	97.33
G_3	220	0	1	0	201	18	91.36
G_4	225	0	0	6	5	214	95.11
Total	604	58	27	78	208	231	94.54

Table 6The performance of HCC classification by using k -NN classifier and all 14 features.

k	Accuracy (%)
1	86.42
3	90.07
5	89.57
7	89.24

8. Conclusions

Accurate grading for hepatocellular carcinoma (HCC) biopsy images is important to prognosis and treatment planning. Visual grading by humans is time-consuming, subjective, and inconsistent while computerized analysis for HCC biopsy images is a very complex task requiring a lot of appropriate image processing steps and experts' domain knowledge for correct grading.

In this paper, we propose an automatic system for grading HCC biopsy images. In image preprocessing, a dual morphological grayscale reconstruction method was proposed to remove noise and accentuate nuclear shapes. Nuclei were segmented from images using marker-controlled watershed transform and GVF active contour method. Such a hybrid approach is robust in terms of removing noise and preserving shapes of nuclei in HCC biopsy images. In feature extraction, 14 features were extracted from segmented biopsy images according to six types of HCC characteristics including nuclear size, nucleocytoplasmic ratio, irregularity, hyperchromatism, anisonucleosis, and nuclear texture. These features comprise both local and global characteristics so that benignancy and different degrees of malignance can be distinguished effectively. In classification, sequential floating forward selection method was used to select an optimal feature subset from the 14 features for the support vector machine associated with every decision node of our decision-graph classifier.

The major contribution of this study is to develop an efficient and effective automated grading system for HCC biopsy images using several novel methods for image preprocessing, feature extraction, and image classification. In particular, a minimum spanning tree model was used to extract features such as degree of clustering among neighboring nuclei which cannot be found explicitly from visual information in the image. The system is efficient because an HCC biopsy image can be classified into a correct grade through four decision steps. The system is very effective because experimental results show that 94.54% of accuracy can be achieved on an average by exercising a set of 804 HCC biopsy images obtained from more than 100 patients. A compact set of 14 features and their quantitative measurements particularly useful for HCC grading are defined in this paper. We also analyzed these 14 features and found that not all of them are equally important or useful at each decision node of our SVM-based decision-graph. The accuracy rate of classification can be promoted from 92.88% to 94.54% if our SVM-based decision-graph classifier was used and a feature subset was carefully selected for each decision node of the classifier as compared to the SVM classifier directly using all 14 features.

Acknowledgments

The authors would like to thank all colleagues in the Department of Pathology at Taichung Veterans General Hospital for providing the sample images and the grading results used in this research study. This research is supported in part by NSC 95-2221-E-005-094 and Ministry of Education, Taiwan, ROC.

References

- [1] H.A. Edmondson, P.E. Steiner, Primary carcinoma of the liver: a study of 100 cases among 48,900 necropsies, *Cancer* 7 (1954) 462–503.

- [2] L.R. Schad, H.P. Schmitt, C. Oberwittler, W.J. Lorenz, Numerical grading of astrocytomas, *Med. Inf.* 12 (1987) 11–22.
- [3] M. Scarpelli, P.H. Bartels, R. Montironi, C.M. Galluzzi, D. Thompson, Morphometrically assisted grading of astrocytomas, *Anal. Quant. Cytol. Histol.* 16 (1994) 351–356.
- [4] M.J. McKeown, D.A. Ramsey, Classification of astrocytomas and malignant astrocytomas by principal component analysis and a neural net, *J. Neuropathol. Exp. Neurol.* 55 (1996) 1238–1245.
- [5] D. Glotsos, et al., A hierarchical decision tree classification scheme for brain tumor astrocytoma grading using support vector machines, in: *Proceedings of Third International Symposium on Image and Signal Processing Analysis*, vol. 2, 2003, pp. 1034–1038.
- [6] Y. Smith, G. Zajicek, M. Werman, G. Pizov, Y. Sherman, Similarity measurement method for the classification of architecturally differentiated images, *Comput. Biomed. Res.* 32 (1999) 1–12.
- [7] K. Jafari-Khouzani, H. Soltanian-Zadeh, Multiwavelet grading of pathological images of prostate, *IEEE Trans. Biomed. Eng.* 50 (2003) 697–704.
- [8] R. Farjam, H. Soltanian-Zadeh, R.A. Zoroofi, K. Jafari-Khouzani, Tree-structured grading of pathological images of prostate, in: *Proceedings of SPIE: Medical Imaging*, vol. 5747, 2005, pp. 840–851.
- [9] A. Tabesh, A.M. Teverovskiy, H.Y. Pang, V.P. Kumar, D. Verbel, A. Kotsianti, O. Saidi, Multifactor prostate cancer diagnosis and gleason grading of histological images, *IEEE Trans. Med. Imaging* 26 (2007) 1366–1378.
- [10] J.R. Hand, A. Broders, Carcinoma of the kidney: the degree of malignancy in relation to factors bearing on prognosis, *J. Urol.* 28 (1931) 199–216.
- [11] S.A. Fuhrman, L.C. Lasky, C. Limas, Prognostic significance of morphologic parameters in renal cell carcinoma, *Am. J. Surg. Pathol.* 6 (1982) 655–663.
- [12] C.M. Lohse, M.L. Blute, H. Zincke, A.L. Weaver, J.C. Cheville, Comparison of standardized and non-standardized nuclear grade of renal cell carcinoma to predict outcome among 2042 patients, *Am. J. Clin. Pathol.* 118 (2002) 877–886.
- [13] T.Y. Kim, H.J. Choi, S.J. Cha, H.K. Choi, Study on texture analysis of renal cell carcinoma nuclei based on the Fuhrman grading System, in: *Proceedings of Seventh International Workshop on Enterprise Networking and Computing in Healthcare Industry*, 2005, pp. 384–387.
- [14] G. Novara, G. Martignoni, W. Artibani, V. Ficarra, Grading systems in renal cell carcinoma, *J. Urol.* 177 (2007) 430–436.
- [15] T.H. Cormen, C.E. Leiserson, R.L. Rivest, C. Stein, *Introduction to Algorithms*, second ed., MIT Press, McGraw-Hill, 2001.
- [16] B.R. Kumar, D.K. Joseph, T.V. Sreenivas, Teager energy based blood cell segmentation, in: *International Conference on Digital Signal Processing*, vol. 2, 2002, pp. 619–622.
- [17] D. Wu, Q. Zhang, A novel approach for cell segmentation based on directional information, in: *Proceedings of First International Conference on Bioinformatics and Biomedical Engineering*, 2007, pp. 920–923.
- [18] R.L. Cahn, R.S. Poulsen, G. Toussaint, Segmentation of cervical cell images, *J. Histochem. Cytochem.* 25 (1977) 681–688.
- [19] F. Schnorrenberg, C.S. Pattichis, K.C. Kyriacou, C.N. Schizas, Computer-aided detection of breast cancer nuclei, *IEEE Trans. Inf. Technol. Biomed.* 1 (1997) 128–140.
- [20] H.S. Wu, J. Barba, J. Gil, Iterative thresholding for segmentation of cells from noisy images, *J. Microsc.* 197 (2000) 296–304.
- [21] B. Liu, C. Yin, Z. Liu, Z. Zhang, J. Gao, M. Zhu, J. Gu, K. Xu, Microscopic image analysis and recognition on pathological cells, in: *Proceedings of 20th Canadian Conference on Electrical and Computer Engineering*, vol. 1022, 2003, pp. 1022–1025.
- [22] J.P. Thiran, B. Macq, Morphological feature extraction for the classification of digital images of cancerous tissues, *IEEE Trans. Biomed. Eng.* 43 (1996) 1011–1020.
- [23] C.D. Ruberto, A. Dempster, S. Khan, B. Jarra, Analysis of infected blood cell images using morphological operators, *Image Vision Comput.* 20 (2002) 133–146.
- [24] J. Angulo, G. Flandrin, Automated detection of working area of peripheral blood smears using mathematical morphology, *Anal. Cell. Pathol.* 25 (2003) 37–49.
- [25] N. Malpica, C.O. de Solorzano, J.J. Vaquero, A. Santos, I. Vallcorba, J.M. Garcia-Sagredo, F. del Pozo, Applying watershed algorithms to the segmentation of clustered nuclei, *Cytometry* 28 (1997) 289–297.
- [26] L. Olivier, E. Abderrahim, C. Hubert, G. Gilles, L. Michel, E. Hubert, R. Marinette, Segmentation of cytological images using color and mathematical morphology, *Acta Stereologica* 18 (1999) 1–14.
- [27] F.B. Tek, A.G. Dempster, I. Kale, Blood cell segmentation using minimum area watershed and circle radon transformations, in: *Proceedings of International Symposium on Mathematical Morphology*, 2005, pp. 441–454.
- [28] A. Garrido, N.P. de la Blanca, Applying deformable templates for cell image segmentation, *Pattern Recognition* 33 (2000) 821–832.
- [29] L. Liu, S. Sclaroff, Medical image segmentation and retrieval via deformable models, in: *Proceedings of the International Conference on Image Processing*, vol. 3, 2001, pp. 1071–1074.
- [30] C. Zimmer, E. Labruyere, V. Meas-Yedid, N. Guillen, J.C. Olivo-Marin, Segmentation and tracking of migrating cells in videomicroscopy with parametric active contours: a tool for cell-based drug testing, *IEEE Trans. Med. Imaging* 21 (2002) 1212–1221.
- [31] M. Hu, X. Ping, Y. Ding, A new active contour model and its application on cell segmentation, in: *Proceedings of Eighth International Conference on Control Automatics, Robotics and Vision*, vol. 2, 2004, pp. 1104–1107.
- [32] F. Zamani, R. Safabakhsh, An unsupervised GVF Snake approach for white blood cell segmentation based on nucleus, in: *Proceedings of Eighth International Conference on Signal Processing*, vol. 2, 2006.
- [33] D.P. Mukherjee, N. Ray, S.T. Acton, Level set analysis for leukocyte detection and tracking, *IEEE Trans. Image Process.* 13 (4) (2004) 562–572.
- [34] M. Kantardzic, *Data mining: Concepts, Models, Methods, and Algorithms*, Wiley, NJ, 2002.
- [35] C. Cortes, V. Vapnik, Support-vector network, *Mach. Learn.* 20 (1995) 273–297.
- [36] V. Vapnik, *The Nature of Statistical Learning Theory*, Springer, New York, NY, 1995.
- [37] P.N. Tan, M. Steinbach, V. Kumar, *Introduction to Data Mining*, Addison-Wesley, 2006.
- [38] S.S. Keerthi, C.J. Lin, Asymptotic behaviors of support vector machines with Gaussian kernel, *Neural Comput.* 15 (2003) 1667–1689.
- [39] R.M. Haralick, S.R. Sternberg, X. Zhuang, Image analysis using mathematical morphology, *IEEE Trans. Pattern. Anal. Mach. Intell.* 9 (1987) 532–550.
- [40] L. Vincent, Morphological grayscale reconstruction in image analysis: applications and efficient algorithms, *IEEE Trans. Image Process.* 2 (1993) 176–201.
- [41] Gonzalez, Woods, *Digital Image Processing*, second ed., Prentice-Hall, 2002.
- [42] J.B.T.M. Roerdink, A. Meijster, The watershed transform: definitions, algorithms and parallelization strategies, *Fundam. Inform.* 41 (2000) 187–228.
- [43] C.M. Chen, H.S. Lu, Y.S. Huang, Cell-based dual snake model: a new approach to extracting highly winding boundaries in the ultrasound images, *Ultrasound Med. Biol.* 28 (2002) 1061–1073.
- [44] M. Kass, A. Witkin, D. Terzopoulos, Snake: active contour models, *Int. J. Comput. Vision* 1 (1987) 321–331.
- [45] C. Xu, J.L. Prince, Snakes, shapes, and gradient vector flow, *IEEE Trans. Image Process.* 7 (1998) 359–369.
- [46] P. Soille, *Morphological Image Analysis*, second ed., Springer, 2003.
- [47] K.G. Ishak, Z.D. Goodman, J.T. Stocker, *Tumors of the Liver and Intrahepatic Bile Ducts*, Armed forces institute of pathology, Washington, DC, 2001.
- [48] U.C. Nzeako, Z.D. Goodman, K.G. Ishak, *Tumor pathology and survival in HCC*, *Cancer* 74 (1995) 579–588.
- [49] H. Kauppinen, T. Seppanen, M. Pietikainen, An experimental comparison of autoregressive and Fourier-based descriptors in 2D shape classification, *IEEE Trans. Pattern. Anal. Mach. Intell.* 17 (1995) 201–207.
- [50] A. Moragas, M. Garcia-Bonafe, I. de Torres, M. Sans, Textural analysis of lymphoid cells in serous effusions. A mathematical morphologic approach, *Anal. Quant. Cytol. Histol.* 15 (1993) 165–170.
- [51] R.M. Haralick, K. Shanmugam, I. Dinstein, Texture features for image classification, *IEEE Trans. Syst. Man Cybern. SMC-3* (1973) 610–621.
- [52] R.M. Haralick, Statistical and structural approaches to texture, *Proceedings IEEE* 67 (1979) 786–804.
- [53] L.G. Shapiro, G.C. Stockman, *Computer Vision*, Prentice-Hall, 2001.
- [54] D. Mayumi, U. Sabino, L.D.F. Costa, E.G. Rizzatti, M.A. Zago, A texture approach to leukocyte recognition, *Real-Time Imaging* 10 (2004) 205–216.
- [55] J.C. Burges, A tutorial on support vector machines for pattern recognition, *Data Min. Knowl. Discovery* 2 (1998) 121–167.
- [56] C.W. Hsu, C.J. Lin, A comparison on methods for multiclass support vector machines, *IEEE Trans. Neural Netw.* 13 (2002) 415–425.
- [57] K. Duan, S.S. Keerthi, Which is the best multiclass SVM method? An empirical study, in: *Proceedings of Multiple Classifier Systems, Lecture Notes in Computer Science* 3541 (2005) 278–285.
- [58] C.C. Chang, C.J. Lin, LIBSVM: a library for support vector machines, 2001, Software available at <<http://www.csie.ntu.edu.tw/~cjlin/libsvm>>.
- [59] P. Pudil, J. Novovicova, J. Kittler, Floating search methods in feature selection, *Pattern Recognition Lett.* 15 (1994) 1119–1125.
- [60] S.D. Stearns, On selecting features for pattern classifiers, in: *Proceedings of Third International Conference on Pattern Recognition*, 1976, pp. 71–75.
- [61] M. Kudo, J. Sklansky, Comparison of algorithms that select features for pattern classifiers, *Pattern Recognition* 33 (2000) 25–41.
- [62] A.K. Jain, R.P.W. Duin, J. Mao, Statistical pattern recognition: a review, *IEEE Trans. Pattern Anal. Mach. Intell.* 22 (2000) 4–37.

About the Author—PO-WHEI HUANG: received his B.S. degree in applied mathematics from National Chung-Hsing University in 1973, the M.S. degree in mathematics from Texas Tech University in 1978, and the Ph.D. degree in computer science from Southern Methodist University in 1989. He was with Texas Instruments in Dallas as a member of technical staff, project manager, and software development manager from 1978 to 1990. He was the department chairman and has been a professor in the Department of Computer Science and Engineering at National Chung-Hsing University. From September 2002 to October 2004, he served as the vice president of National Huwei University of Science and Technology located in Yunlin County of Taiwan. From October 2004 to January 2006, he was appointed as the Secretary General of National Chung-Hsing University. Since February 2006, he has been the dean of College of Science at National Chung-Hsing University. He was elected as a distinguished professor of National Chung Hsing University in 2007. His research interests include image database, computer vision, pattern recognition, and artificial intelligence.